Ru nanoparticles deposited on ultrathin TiO_2 nanosheets as highly active catalyst for levulinic acid hydrogenation to γ-valerolactone

Xiaoqing Gao[a,b], Shanhui Zhu[a,*], Mei Dong[a], Jianguo Wang[a], Weibin Fan[a,*]

[a] *State Key Laboratory of Coal Conversion, Institute of Coal Chemistry, Chinese Academy of Sciences, Taiyuan 030001, PR China*
[b] *University of Chinese Academy of Sciences, Beijing 100039, PR China*

ARTICLE INFO

ABSTRACT

Highly efficient synthesis of valuable γ-valerolactone (GVL) by levulinic acid (LA) hydrogenation is still a challenge for Ru-based catalysts under mild condition. In this work, we have reported that ultrathin TiO_2 nanosheets supported Ru nanoparticles showed extraordinarily high catalytic activity, GVL yield (99.1%) and reusability owing to the formation of Ru−O−Ti interfacial structure. The turnover frequency (TOF) reached as high as $19,045\ h^{-1}$ at 100 °C, much higher than those of Ru/SiO_2, Ru/GO, Ru/MoS_2, and commercial Ru/C. DFT calculation elucidates that the dominant reaction pathway of LA hydrogenation to GVL is preferentially hydrogenated to $CH_3CHOCH_2CH_2COOH^*$, followed by cyclization to $CH_3(OH)C_4OH_4OH^*$ (GVL − OH) and final dehydroxylation, irrespective of surface structure. Compared to Ru (0 0 2) facet, Ru/TiO_2 interfacial structure changes the rate-determining step from initial hydrogenation to cyclization, which greatly declines the activation barrier from 0.81 eV to 0.48 eV.

1. Introduction

Highly effective transformation of renewable biomass-feedstocks, including platform chemicals, is becoming increasingly attractive in sustainable production of biofuels and fine chemicals. Levulinic acid (LA), produced abundantly from the decomposition of cellulose or sugars, is a versatile platform chemical for synthesizing a variety of valuable derivatives [1–4]. Sustainable production of γ-valerolactone (GVL) via hydrogenation is regarded as one of the most desired strategies in the valorisation of LA. GVL has been identified as a promising feedstock for the production of transportation fuels or directly used as fuel additive [5,6]. Recently, it has been demonstrated as an important solvent in biomass transformation for the dissolution of cellulose and humins [7].

Abundant supported metal catalysts, including Ru [8–22], Pt [11], Pd [23,24], Ir [25], Cu [26,27], Co [28], Ni [29–34], or bimetallic metals [35–38], have been frequently employed for LA hydrogenation to GVL. Of them, Ru-based catalysts generally afforded excellent activity and selectivity for producing GVL owing to their intrinsically superior ability to activate carbonyl groups. A variety of supports, including TiO_2 [8,11,14], ZrO_2 [8,17], graphene [9,10], hydroxyapatite [24] or carbon [15], have been reported to show high performance by loading Ru nanoparticles. Li et al. [36] fabricated a highly dispersed Ru-Ni bimetallic catalyst embedded in mesoporous carbon and obtained a

97% yield of GVL with 15 times catalytic cycles without obvious loss in activity. Huang et al. [10] achieved 99.7% LA conversion and 100% GVL selectivity along with a GVL production rate of 365 $mol_{GVL}\ g_{Ru}^{-1}\ h^{-1}$ in few-layer graphene supported Ru. Weckhuysen et al. [8] disclosed that Ru/ZrO_2 maintained near-quantitative yields of GVL upon multiple recycling in comparison with severe deactivated Ru/TiO_2 and Ru/C. Regardless of their great advances, most of previous studies mainly focus on catalytic performance (activity, selectivity and stability) or structure-performance correlation, while the complex reaction mechanism has been less deeply investigated on Ru/support interface owing to the limitation of experimental techniques. Moreover, the catalysts that their intrinsic catalytic activity can surpass 10,000 $mol_{LA}\ mol_{metal}^{-1}\ h^{-1}$ have been scarcely reported under mild conditions.

Density functional theory (DFT) calculation has been demonstrated to be a powerful strategy in the rational design of metal-oxide support interface structure to explore the surface reaction mechanism. The interface structure directly participates in the catalytic cycle by adsorbing and activating reactants as well as intermediates. For example, Honkala et al. [39] used DFT calculation to modelling the Rh-ZrO_2 interface for water-gas shift reaction. The interface can activate water to form hydroxyl group that is apt to react with CO adsorbed on adjacent Rh sites. Although some papers [40,41] have conducted DFT method to explore the reaction mechanism of LA hydrogenation to GVL on Ru (0001)

* Corresponding authors.
E-mail addresses: zhushanhui@sxicc.ac.cn (S. Zhu), fanwb@sxicc.ac.cn (W. Fan).

facet, no related work has been reported to elucidate the critical role of metal-support interface.

Ultrathin nanosheets have recently drawn great attention due to their high density unsaturated atoms exposed on the surface and unique two dimensional (2D) structure [42–44]. Compared to complex 3D microporous or mesoporous materials, 2D nanosheets can be used as promising support to anchor metal in order to explore reaction mechanism on Ru/support interface. Additionally, to improve the intrinsic activity of Ru-based catalysts for LA hydrogenation, we searched for many typical support, including 2D TiO_2, MoS_2 and graphene oxide (GO). Among them, TiO_2 nanosheets formed strong interface interaction with Ru nanoparticles and exhibited unprecedented intrinsic activity as high as $19,045\,h^{-1}$ for LA hydrogenation to GVL, which was the highest value ever reported. According to DFT calculation results, the enhanced activity of Ru/TiO_2 is closely correlated with the Ru−O−Ti interface structure by its direct participation in LA hydrogenation. Specifically, Ru/TiO_2 interfacial structure tunes the rate-determining step from initial LA hydrogenation to $CH_3CHOCH_2CH_2COOH^*$ cyclization, which significantly decreases the activation barrier from 0.81 eV to 0.48 eV.

2. Experimental

2.1. Catalyst preparation

TiO_2 nanosheets were prepared by a modified hydrothermal method [45]. 5 mL tetrabutyl titanate (Energy Chemical) and 1.0 mL hydrofluoric acid solution (40 wt.%, Sinopharm Chemical Reagent Co., Ltd., China (SCRC)) were mixed together in a 25 mL Teflon-lined stainless steel autoclave under stirring conditions for 10 min. Subsequently, the autoclave was statically kept in 200 °C for 24 h, and then naturally cooled to room temperature. The mixture was repeatedly centrifugated with ethanol and water, and the collected solid was dried at 80 °C overnight.

GO was prepared by a modified Hummer's method [46]. 5 g graphite and 2.5 g $NaNO_3$ were added into 115 mL 98 wt.% H_2SO_4 with vigorous stirring in an ice-water bath. After the introduction of 15 g $KMnO_4$, the mixture was heated into 35 °C and continued to stir for 30 min, followed by the addition of 230 mL deionized water. The above suspension was heated to 98 °C, diluted by additional 700 mL deionized water and introduced 50 mL H_2O_2. The graphite oxide was collected by filtration, washing and drying at 50 °C. At last, GO was obtained by sonication exfoliation for 60 min.

For the preparation of MoS_2, 2 mmol $(NH_4)_2Mo_2O_7\cdot 4H_2O$ (SCRC) and 28 mmol thiourea (Aladdin) were added into 70 mL water under vigorous stirring for 10 min. Subsequently, the mixed solution was heated at 220 °C for 21 h. Subsequently, the MoS_2 nanosheets were collected by filtration, washing and drying at 80 °C.

For Ru/TiO_2, 0.2 g TiO_2 was added into 10 mL $RuCl_3$ (0.004 mol/L SCRC) aqueous solution and stirred vigorously for 1 h. 2.37 mL $NaBH_4$ (SCRC) solution (0.25 mol/L) was dripped into the above mixture under stirring condition for 30 min. Subsequently, the solid catalyst was separated by centrifugation and dried overnight at 80 °C. Other supported catalysts were synthesized with the same method as above. Ru/C was commercially obtained from Aladdin. TiO_2-P25 was purchased from Degussa (Germany). Ru contents were checked by inductively coupled plasma-optical emission spectroscopy (ICP-OES) measurements, as displayed in Table 1.

2.2. Catalyst characterization

N_2 adsorption-desorption isotherms were collected on at −196 °C on a Micromeritics TriStar 3000 instrument. Prior to the measurements, the samples were pretreated under vacuum at 250 °C for 8 h. ICP-OES was employed to detect the Ru content. X-ray diffraction (XRD) was carried out in a Rigaku Miniflex II desktop X-ray diffractometer with a

Table 1
The physicochemical property and turnover frequency (TOF) value of various supported Ru-based catalysts.

Catalyst	BET surface area	Ru content (%)	Ru size (nm)	Dispersion (%)	TOF (h^{-1})
Ru/TiO_2	67.5	0.83	1.4	92.1	19,045
Ru/SiO_2	115.9	0.97	2.1	61.4	7089
Ru/MoS_2	25.8	0.76	2.0	64.5	693
Ru/GO	85.3	0.81	1.7	75.9	11524
Ru/C	–	5.0	2.7	47.8	1909

Cu Kα radiation source at 40 kV and 40 mA. Scan speed was set as 4°/min in the 2θ range of 5° and 90°. Transmission electron microscopy (TEM) and high-resolution transmission electron microscopy (HRTEM) measurements were performed on a JEM 2011 F instrument operated at 200 kV voltages. Samples were dispersed onto a carbon coated copper grid after 20 min ultrasonic treatment. X-ray photoelectron spectroscopy (XPS) was performed on a Kratos AXIS ULTRA DLD spectrometer with Al Kα radiation under ultrahigh vacuum conditions. Temperature-programmed reduction of hydrogen (H_2-TPR) was performed on Micromeritics Autochem 2920. After pretreatment in Ar at 300 °C for 0.5 h, the cooled sample was heated from 30 °C to 500 °C at a ramp of 5°/min in 10 vol% H_2/Ar and the consumed H_2 was monitored by a thermal conductivity detector (TCD). More experimental conditions have been provided in Supplementary Information.

2.3. Catalytic tests

Typically, 2 mmol LA, 4 mL water and 0.005 g catalyst were charged into a 10 mL Teflon-lined stainless steel autoclave (NS-10-316 L, Anhui Kemi Machinery Technology Co., Ltd.). Prior to a reaction test, the autoclave was purged with H_2 for 5 times, pressurized into 4 MPa and heated into 100 °C. After the reaction test was terminated for desired time, the reaction system was cooled down in an ice-water bath. Subsequently, the liquid products were separated by centrifugation and analysed by gas chromatography (Shimadzu GC-2010) with a flame ionization detector using a DB-1 capilliary column (60 m × 0.25 mm × 0.25 μm). All the products were identified by GC–MS.

Turnover frequency (TOF) in the conversion of LA was calculated based on surface Ru atoms at initial reaction time. The surface Ru atoms were estimated on total Ru atoms and Ru dispersion. According to earlier reports [38,47], Ru dispersion (D) can be calculated by the equation $D = \frac{6 \times V}{a \times d}$, in which V is the volume of per Ru atom ($0.01365\,nm^3$), a is the surface area per Ru atom ($0.0635\,nm^2$), and d refers to Ru average particle size in nm from TEM counting.

$$TOF = \frac{Mole\ number\ of\ converted\ LA}{Number\ of\ surface\ Ru\ atoms \times reation\ time}$$

2.4. DFT calculations

All calculations were performed in Vienna ab initio simulation package (VASP) with plane-wave-based periodic DFT method [48,49]. The exchange and correlations energies were described by Perdew, Burke, and Ernzerhof (PBE) functional [50], while the core electrons of elements were treated by the projector augmented wave (PAW) setups [51,52]. The cutoff energy was set as 450 eV and the $3 \times 3 \times 1$ Monkhorst-Pack k-points were employed.

Based on XRD and TEM results, the most exposed Ru (0 0 2) facet was modeled using a four-layer periodic slab with 4×4 supercell (Fig. 1). The Ru/TiO_2 interface was modeled with a 10 Ru atoms clusters bound to anatase TiO_2 (1 0 1) facet [53], in which 3×2 supercell with 5 layer slab was used to describe TiO_2. Anatase TiO_2 (1 0 1) facet was chosen because our Ru/TiO_2 catalyst predominantly exposed (1 0 1) surface. The electronic structure of Ti was modeled with DFT + U method with a U value of 2.

Adsorption energy (E_{ads}) of adsorbate was calculated based on the
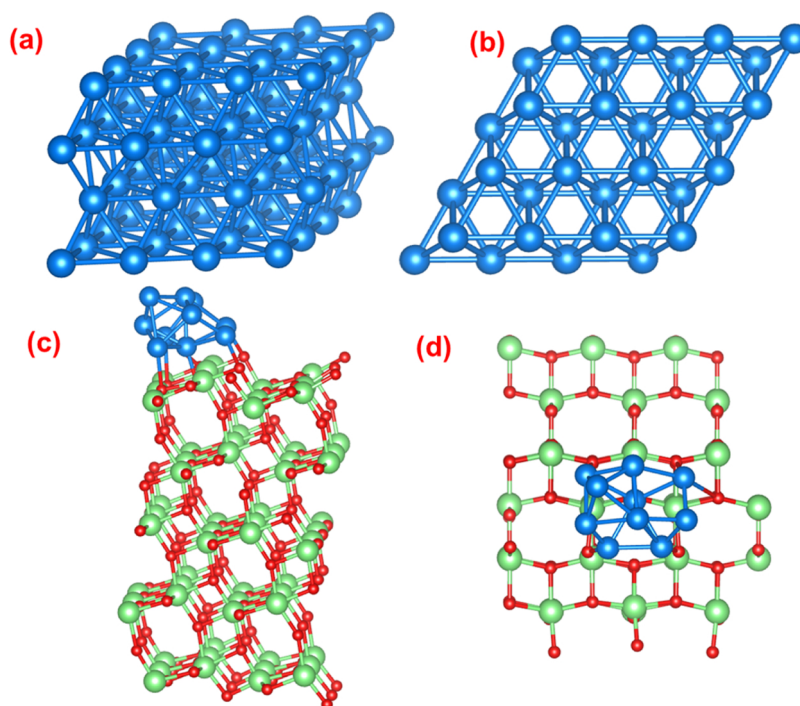
Fig. 1. Side (a and c) and top view (b and d) of Ru (0 0 2) facet and Ru_{10}/TiO_2 (101) models, respectively. Blue, red, and green balls represent Ru, O, and Ti atoms, respectively. (For interpretation of the references to colour in this figure legend, the reader is referred to the web version of this article).

most stable structure, relative to clean slab (E_{slab}) and substrate molecule (E_{sub}). The calculation equation of E_{ads} is described as $E_{ads} = E_{sub/slab} - E_{slab} - E_{sub}$, in which $E_{sub/slab}$ is the total energy of adsorbed substrate on slab model. The transition states (TSs) were determined by a climbing image nudged elastic band (CI-NEB) method [54–56], and verified by the presence of a single imaginary vibrational mode along the reaction coordinate. Activation energy (E_a) of elementary reaction was estimated by the energy difference between TS and initial state (IS). Reaction energy (E_r) was calculated by the energy difference between final state (FS) and IS.

3. Results and discussion

3.1. Catalyst characterization

As illustrated in Fig. 2, the TEM images show that the as-prepared

TiO_2 presents well-defined rectangle nanosheets morphology with their length in the range of 80–140 nm. The ultrathin feature can be easily discerned by the HRTEM image with 5–7 nm in thickness. HRTEM image indicates that the most exposed facet is (1 0 1) of anatase TiO_2, as confirmed by a lattice spacing of 0.35 nm [45]. XRD patterns of pure TiO_2 (Fig. S1) showed noticeable diffraction peaks at 25.4°, 38.2°, 48.3°, 54.2°, 55.3°, 62.8°, 70.5°, 75.6°, and 76.5°, which are assigned to the (101), (004), (200), (105), (211), (204), (220), (215), and (301) lattice planes of the anatase TiO_2 [45], respectively.

After deposition of Ru nanoparticles, the morphology of TiO_2 nanosheets did not change (Fig. 3). Ru nanoparticles were uniformly distributed on the surface of TiO_2 nanosheets. HRTEM (Fig. 3d) shows that Ru nanoparticles were directly connected to TiO_2 without any transitions layers, an indication of forming strong anchoring interface. These interfacial regions were rather robust, as evidenced by the clear distinction of Ru (0 0 2) [57] and TiO_2 (1 0 1) [58] lattice fringes. The
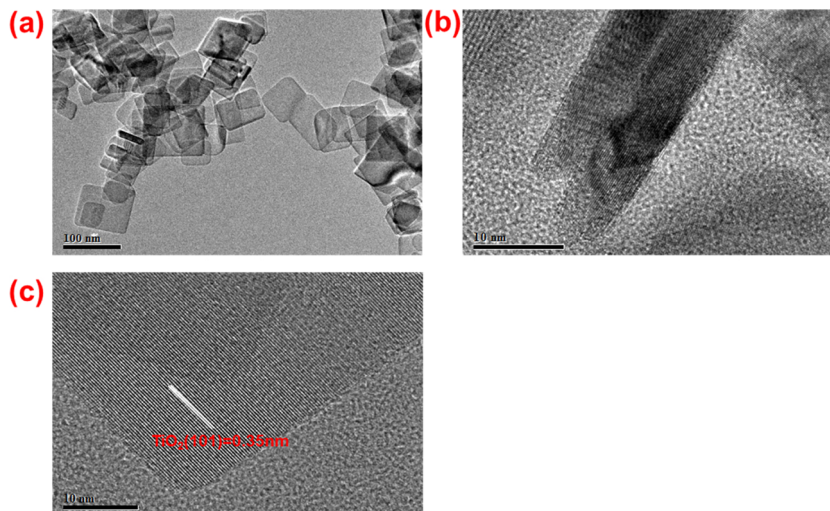
Fig. 2. (a–c) TEM and HRTEM images of TiO_2. Fig. 3. (a–d) TEM and HRTEM images of Ru/TiO_2; (e) Ru nanoparticles size distribution histogram of Ru/TiO_2.
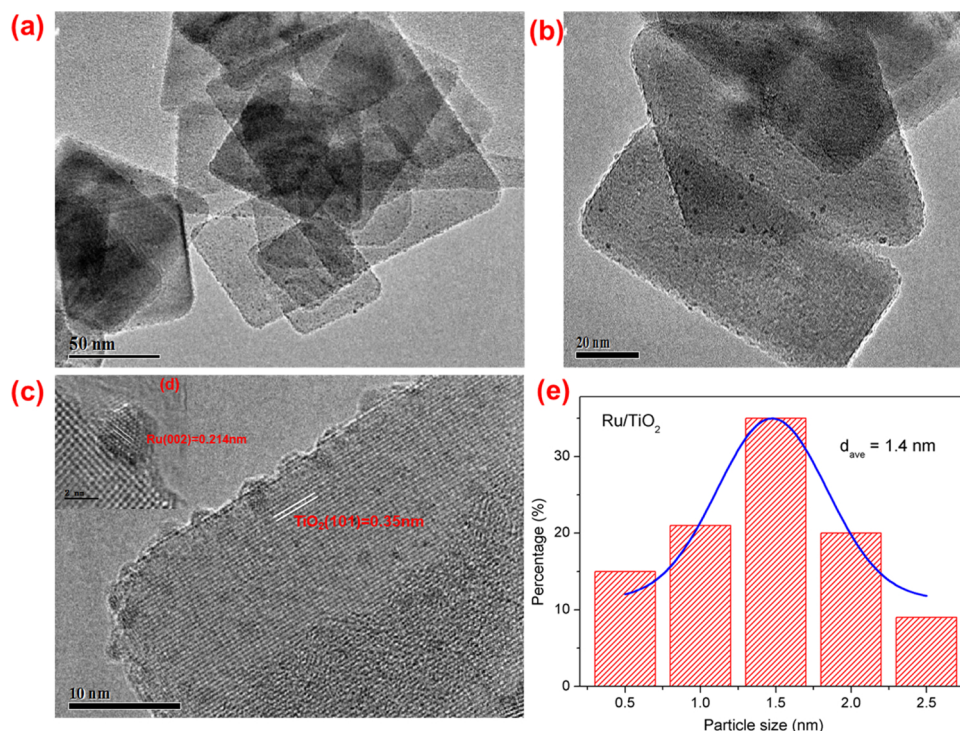
Fig. 3. (a–d) TEM and HRTEM images of Ru/TiO$_2$; (e) Ru nanoparticles size distribution histogram of Ru/TiO$_2$.

statistical analysis shows a very narrow particle size distribution of Ru nanoparticles and the average Ru particle size is only 1.4 nm. XRD patterns of Ru/TiO$_2$ did not detect any diffraction peaks of Ru, also suggesting their highly dispersed states. N$_2$ physical adsorption in Table 1 shows that Ru/TiO$_2$ possesses a 67.5 m^2/g BET surface area.

We also employed a series of other supports, including SiO$_2$, 2D MoS$_2$ and GO, to prepare supported Ru catalysts. As shown in Fig. S2, small Ru nanoparticles were homogenously distributed on SiO$_2$ surface, and the average size of Ru nanoparticles was 2.1 nm. Fine and well dispersed Ru nanoparticles were also distributed on MoS$_2$ (Fig. S3) and GO (Fig. S4) nanosheets, and their average sizes of Ru nanoparticles were only 2.0 nm and 1.7 nm, respectively. However, no obvious interface structure was observed on SiO$_2$, MoS$_2$ and GO supported Ru catalysts, which may be the weak interaction between Ru and support. Additionally, XRD patterns in Fig. S1 only show the diffraction peaks of support, also confirming the homogenously dispersed Ru nanoparticles on support.

Fig. 4a shows the H$_2$-TPR profiles of various Ru-based catalysts. For all the catalysts, two reduction reigns were observed, namely low temperature at 75 °C ~150 °C and high temperature range at 160 °C ~250 °C. The H$_2$ reduction peak of low temperature was probably

related to the weakly interacted Ru nanoparticles or surface Ru species [14]. Ru/GO displayed a very broad H$_2$ reduction peak along with two shoulder peaks in the range of 75 °C ~150 °C, indicated the various Ru states owing to the abundant oxygen-containing groups of GO [46]. Additionally, the H$_2$ reduction peak of high temperature was probably ascribed to the Ru nanoparticles with relatively strong interaction with the support [14]. For Ru/TiO$_2$, its reduction temperature of high temperature peak was obviously higher than other samples, suggesting that the Ru-TiO$_2$ interaction was much stronger.

Fig. 4b displays the Ru 3d and C 1s peaks of XPS spectra of various supported Ru-based catalysts. Owing to the serious overlapping of C 1s and Ru 3d$_{3/2}$ peaks in the range of 283.3 and 286.8 eV, the Ru 3d$_{5/2}$ peak is used to identify their chemical states. For GO, SiO$_2$ and MoS$_2$ supported Ru, the peak at 280.4 eV is attributed to Ru 3d$_{5/2}$ of Ru^0 [19]. This peak shifted remarkably to 280.8 eV along the direction of high binding energy over Ru/TiO$_2$, indicating that electron transfer occurred from Ru^0 to TiO$_2$ owing to their strong interfacial interaction. The formation of strong interface interaction between Ru and TiO$_2$ is also verified by TEM results, in also line with previous report [59] that strong Ru-TiO$_2$ interaction on the defect-rich TiO$_2$ (1 0 1) facet not only stabilizes hemispherical Ru nanoparticles, but also leads to electronic
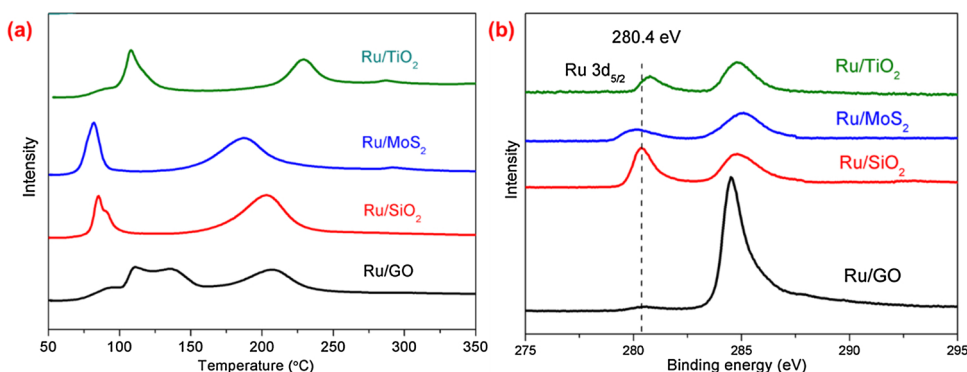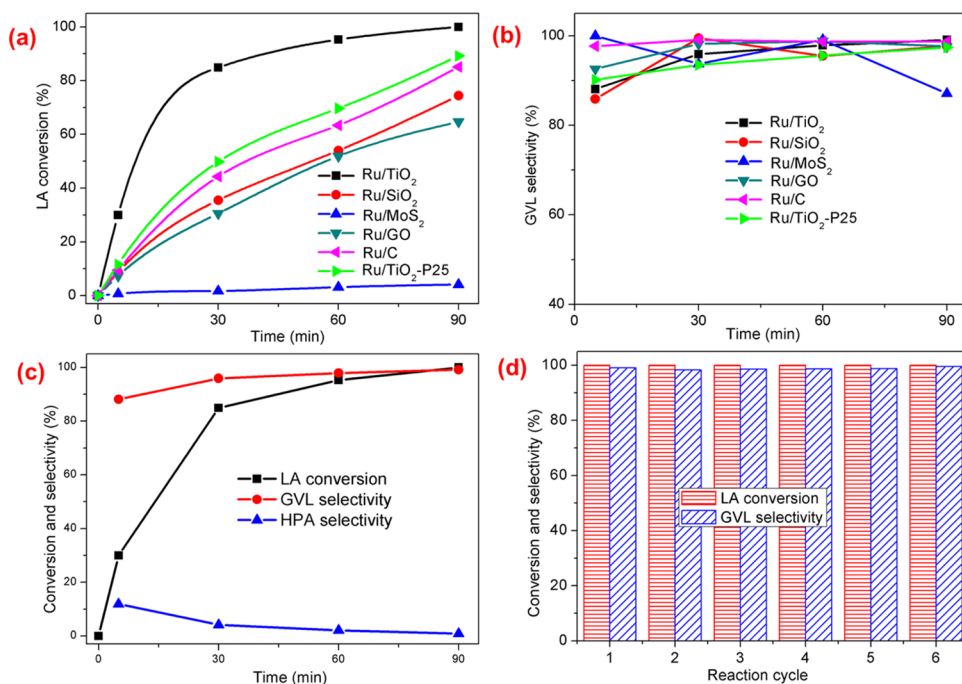

Fig. 4. (a) H$_2$-TPR and (b) XPS spectra of various supported Ru-based catalysts.

Fig. 5. (a and b) Catalytic performance of LA hydrogenation to GVL over various Ru-based catalysts. (c) Product distribution of LA conversion as a function of time over Ru/TiO$_2$. (d) Reusability tests of LA conversion over Ru/TiO$_2$. Reaction conditions: 0.005 g catalyst, 2 mmol LA, 4 MPa H$_2$, 100 °C, 4 mL water or 90 min only for (d).

modifications of surface Ru atoms.

3.2. Catalytic performance of LA hydrogenation

Fig. 5a and b illustrate the catalytic performance of LA hydrogenation at 100 °C over various supported Ru catalysts. Generally, all of the catalysts gave fairly high GVL selectivity (> 85.9%), suggesting that the formation of by-product 4-hydroxypentanoic acid (HPA) is greatly suppressed. However, the reaction activity varied significantly. Ru/MoS$_2$ gave very poor activity, only 4.1% conversion of LA even at 90 min reaction time. Comparatively, moderate conversion of LA was obtained over Ru/SiO$_2$ and Ru/GO, being 74.4% and 64.7% at 90 min, respectively. Many previous reports [8,16] have demonstrated that the commercial Ru/C exhibited good catalytic performance for LA hydrogenation to GVL and were usually employed as a benchmark catalyst. Indeed, Ru/C reached good conversion of LA, up to 85.1% under our reaction condition. TEM images (Fig. S5) showed that Ru nanoparticles were widely distributed from 1 nm to 5 nm with an average Ru particle size of 2.7 nm. Besides, the commercial TiO$_2$-P25 was also used to support Ru for comparison. Under the identical conditions, Ru/TiO$_2$-25 presented good performance of LA hydrogenation or even better than Ru/C. However, LA conversions of Ru/TiO$_2$-25 were always lower than those of TiO$_2$ nanosheets supported Ru in all the tests with different reaction time. Among all the examined catalysts, Ru/TiO$_2$ reached the best performance, up to complete conversion and 99.1% selectivity of GVL at 90 min. With increasing reaction time (Fig. 5c), both LA conversion and GVL selectivity enhanced steadily along with decreasing HPA selectivity. In addition, the Ru/TiO$_2$ catalyst presented exceptional stability in a six-cycle experiments without an obvious loss of activity and GVL selectivity (Fig. 5d). The deactivation of catalyst may be masked at 100% conversion of LA, and thus the recycling tests of Ru/TiO$_2$ were further performed at a moderate conversion (84.9%) by decreasing the reaction time from 90 min to 30 min. The reaction results of reusability tests are illustrated in Fig. S6. The LA conversion and GVL selectivity kept stable for 6 reaction cycles, definitely confirming the robust structure of Ru/TiO$_2$.

The kinetic study on the hydrogenation of LA was rigorously investigated by the analysis of initial reaction rate in the range of 40 °C–100 °C (Fig. 6).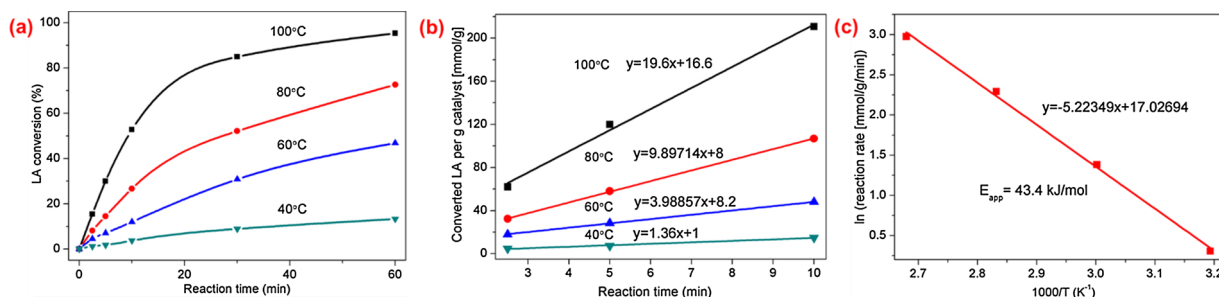 The apparent activation energy (E$_{app}$) of Ru/TiO$_2$ was estimated to be only 43.4 kJ/mol, much lower than that of well-known Ru-based catalysts, such as Ru/RGO (66.01 kJ/mol) [9], Ru/C (87.66 kJ/mol) [9] and nanoporous Ru (65.88 kJ/mol) [57]. The different E$_{app}$ values are indicative of the formation of different active sites.

TOF can be used to reflect the intrinsic activity of a catalyst based on accessible surface Ru atoms. As displayed in Table 1, Ru/TiO$_2$ achieved excellent TOF value, being 19,045 h^{-1} at 100 °C. Moreover, the TOF value of Ru/TiO$_2$ is 10 times higher than that of benchmark catalyst Ru/C (1909 h^{-1}). To the best of our knowledge, the TOF of Ru/TiO$_2$ is the highest value for LA hydrogenation to GVL reported to date (Table S1) [8–10,15,36], and gerernally increases one or two orders of magnitude under similar conditions. Moreover, many previous catalysts were performed under very high temperature, but still gave low TOF value in comparison to our Ru/TiO$_2$, such as Ru/HAP at 275 °C (10,440 h^{-1}) [6], 3Cs-Ru/Al$_2$O$_3$ at 220 °C (2844 h^{-1}) [19], and AuPd/TiO$_2$ at 200 °C (360 h^{-1}) [38]. Obviously, such outstanding catalytic performance and low apparent activation energy in the selective hydrogenation of LA to GVL has demonstrated that nanosheet TiO$_2$ supported Ru is an unprecedentedly excellent catalyst.

The particle size effect cannot be the main factor that affects the reaction performance since TiO$_2$, SiO$_2$, MoS$_2$ and GO supported catalysts present similar Ru nanoparticles distribution with average particle size in the range of 1.4 nm–2.1 nm. In addition, the calculation of TOF is based on the accessible surface Ru atoms, which has excluded the effect of particle size. Thus, the huge difference in reactivity is strongly related to the intrinsic structure. As revealed by H$_2$-TPR, TEM and XPS, Ru atoms are chemically bonded with TiO$_2$ support to form Ru−O−Ti bond, resulting in strong interfacial interaction. In contrast, the Ru atoms are weakly interacted with SiO$_2$, MoS$_2$ and GO but relatively strongly coordinated with the neighbouring Ru atoms. To explore the different roles of Ru nanoparticles and interfacial Ru−O−Ti structure, DFT calculations were further employed to investigate intrinsic catalytic mechanism of LA hydrogenation to GVL at the atomic level.

3.3. Reaction mechanism of LA hydrogenation by DFT calculations

As discussed above, Ru (0 0 2) facet and Ru$_{10}$/TiO$_2$ models were chosen to represent Ru nanoparticles and strong interfacial Ru−O−Ti

Fig. 6. Kinetic behaviour and estimation of apparent activation energy of LA conversion over Ru/TiO$_2$. Reaction conditions: 0.005 g Ru/TiO$_2$, 2 mmol LA, 4 MPa H$_2$, and 4 mL water.
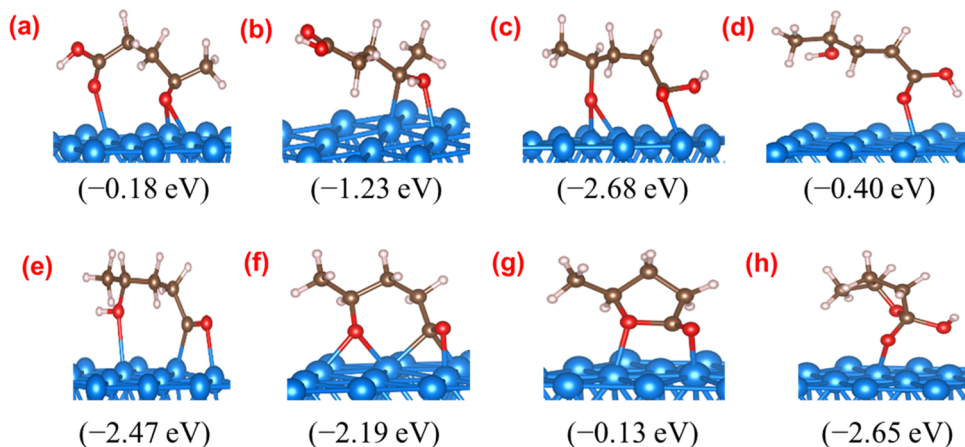
structure in DFT calculations. Generally, the reaction network for LA hydrogenation to GVL undergoes first the hydrogenation of LA to HPA followed by its cyclization [24,60]. Recently, a new pathway with low activation energy barrier has been proposed by Andreas et al. [40], in which LA initially hydrogenates to an alkoxy intermediate CH$_3$CHOCH$_2$CH$_2$COOH, proceeds to ring closure to generate CH$_3$(OH)C$_4$OH$_4$OH (GVL−OH) and finally removes hydroxyl group. Thus, these two pathways were preferentially considered in our DFT calculations. Even some reports [61,62] have confirmed the formation of angelica lactone from LA intraesterification and insisted that angelica lactone can further undergo hydrogenation to produce GVL. However, we did not detect angelica lactone in product mixture. Moreover, Heyden et al. [41] have demonstrated that the reaction pathway of angelica lactone is not a dominant reaction pathway based on DFT calculations and microkinetic model. Therefore, the reaction pathway of angelica lactone is not conducted by DFT modelling.

The adsorbed states of all the possible species were initially calculated in Figs. 7 and 8, Tables S2 and S3. The binding mode nomenclature η$_i$μ$_j$ indicates that i atoms of the adsorbate are bonded to j atoms of Ru sites. LA adsorbs on Ru (0 0 2) facet in a η$_2$μ$_3$ (O, O) mode with a very low adsorption energy of −0.18 eV, suggesting its weak physical adsorption on Ru (0 0 2) surface. However, strong chemical adsorption of LA is identified on the corner Ru sites in Ru$_{10}$/TiO$_2$. Its adsorption energy reaches as high as −0.90 eV. Similar geometry configurations of GVL are observed on Ru (0 0 2) and Ru$_{10}$/TiO$_2$, but with great difference in adsorption energy (−0.13 eV vs −0.65 eV), which should be related to the different Ru sites. The two O atoms weakly binds on surface Ru sites on Ru (0 0 2) facet, while they prefers to adsorb interfacial Ru sites that are bound to O−Ti bond on Ru$_{10}$/TiO$_2$ model. For other species (for example, CH$_3$CHOCH$_2$CH$_2$COOH*, HPA* and GVL−OH*), the O atoms also tend to bind on interfacial Ru sites, despite with similar adsorption energy with those of Ru (0 0 2). Therefore, the interfacial Ru−O−Ti structure is likely to play an important role in activating these species. However, surface Ru site prefers to adsorb H*

and H$_2$* in comparison with interfacial Ru. Moreover, the dissociation of H$_2$* preferentially occurs on surface Ru sites, irrespective of on Ru (0 0 2) or Ru$_{10}$/TiO$_2$.

Fig. 9 shows the reaction diagram of LA hydrogenation to GVL on the surface of Ru (0 0 2) facet. H$_2$ is dissociated very easily on Ru sites and has nearly no activation energy. The adsorbed LA can proceed to hydrogenation of carbonyl group either by initial C−H bond formation to CH$_3$CHOCH$_2$CH$_2$COOH* or O−H bond formation to CH$_3$COHCH$_2$CH$_2$COOH*. With much lower activation energy of 0.81 eV, C−H bond formation is preferred over O−H bond formation, in line with previous results of the hydrogenation of ketones [63]. Subsequently, CH$_3$CHOCH$_2$CH$_2$COOH* undergoes further hydrogenation to generate HPA with a rather high activation energy of 1.22 eV. Even so, the formation of HPA is kinetically preferred via initial C−H bond formation followed by O−H bond formation to that of opposite sequence. HPA is a stable product with a desorption energy of 0.40 eV that is mildly higher than its conversion (0.27 eV) in energy, resulting in the detection of minor product. Subsequently, HPA undergoes sequential dehydroxylation and dehydrogenation to form CH$_3$CHOCH$_2$CH$_2$CO*, which needs low activation barrier for this thermodynamically favourable pathway. The formed CH$_3$CHOCH$_2$CH$_2$CO* performs cyclization to produce desired GVL. Notably, the formation of GVL is kinetically and thermodynamically unfavourable (E$_a$ = 1.21 eV and E$_r$ = 0.69 eV), which promotes us to consider other favourable reaction pathway.

As mentioned above, the formation of GVL can derive from CH$_3$CHOCH$_2$CH$_2$COOH that directly proceeds to cyclization to generate GVL−OH followed by its dehydroxylation. The formation of GVL−OH* needs moderate activation barrier (0.69 eV), while the dehydroxylation of GVL−OH* only requires very low activation energy of 0.13 eV. In this route, the determining-rate step is LA hydrogenation to CH$_3$CHOCH$_2$CH$_2$COOH* with 0.81 eV over Ru (0 0 2) surface. Obviously, this route is significantly superior to HPA pathway in the formation of GVL. In the reaction results of Ru/GO, Ru/SiO$_2$ and Ru/

(a) (−0.18 eV)   (b) (−1.23 eV)   (c) (−2.68 eV)   (d) (−0.40 eV)

(e) (−2.47 eV)   (f) (−2.19 eV)   (g) (−0.13 eV)   (h) (−2.65 eV)

Fig. 7. Adsorption configuration and adsorption energy of the most stable species on Ru (002) facet optimized by DFT calculation. (a) LA; (b) CH$_3$COHCH$_2$CH$_2$COOH; (c) CH$_3$CHO-CH$_2$CH$_2$COOH; (d) HPA; (e) CH$_3$CHOHCH$_2$-CH$_2$CO; (f) CH$_3$CHOCH$_2$CH$_2$CO; (g) GVL (h) GVL − OH. The blue, brown, red and white balls represent Ru, C, O and H atoms, respectively. (For interpretation of the references to colour in this figure legend, the reader is referred to the web version of this article).
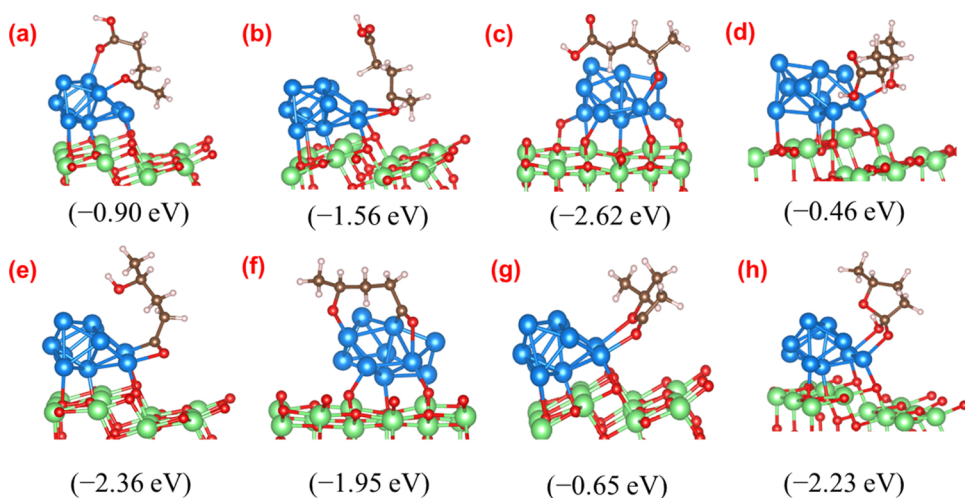
Fig. 8. Adsorption configuration and adsorption energy of the most stable species on Ru_{10}/TiO_2 optimized by DFT calculation. (a) LA; (b) $CH_3COHCH_2CH_2COOH$; (c) $CH_3CHOCH_2CH_2COOH$; (d) HPA; (e) $CH_3CHOHCH_2CH_2CO$; (f) $CH_3CHOCH_2CH_2CO$; (g) GVL (h) GVL − OH. The blue, green, brown, red and white balls represent Ru, Ti, C, O and H atoms, respectively. (For interpretation of the references to colour in this figure legend, the reader is referred to the web version of this article).
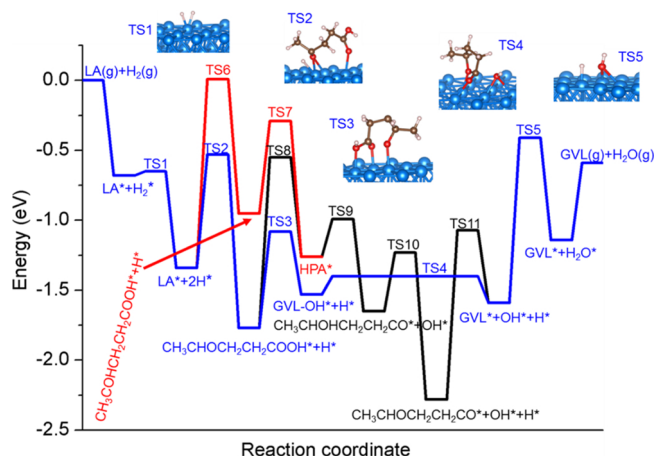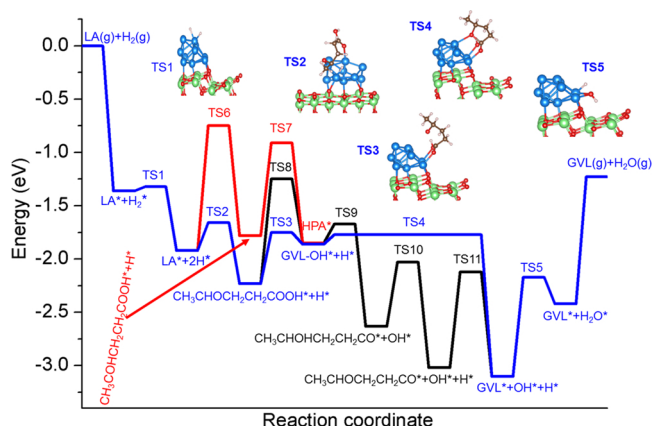

Fig. 9. Potential energy profiles of LA hydrogenation to GVL on Ru (0 0 2) surface.

Fig. 10. Potential energy profiles of LA hydrogenation to GVL on Ru_{10}/TiO_2 surface.

MoS_2, HPA is only formed with low selectivity even at the initial reaction stage of LA hydrogenation, also suggesting that the generation of GVL via HPA should be a minor route. Notably, the remaining OH* from GVL−OH* dehydroxylation will react with nearby H* to produce H_2O* with rather high activation barrier (1.18 eV). Additionally, our DFT calculations results on Ru (0 0 2) is well consistent with the report by Heyden et al. [40] on Ru (0 0 0 1) facet in the case of the dominant reaction pathway and similar activation energy barrier.

Based on our reaction trends, metal-support interface is probably involved and plays a important role in the catalytic cycle of LA hydrogenation. However, no earlier reports [40,41] disclose the reaction mechanism on the interface structure. Thus, we have constructed a Ru_{10}/TiO_2 interfacial structure to explore the possible elementary reactions of LA hydrogenation. In agreement with the calculation results of Ru (0 0 2) and previous Ru (0 0 0 1) [40] models, the present DFT study (Fig. 10) also shows the preferred formation of GVL − OH + dehydroxylation pathway on Ru_{10}/TiO_2 via $CH_3CHOCH_2CH_2COOH$* and GVL − OH* intermediates over the HPA pathway for LA hydrogenation to GVL. On Ru_{10}/TiO_2, the stabilization of reaction intermediates involved in LA hydrogenation requires Ru, O, or the synergy of both sites, and the Ru-TiO₂ interface likely provides multiple activation sites for the reaction. The adsorbed $CH_3CHOCH_2CH_2COOH$* on Ru of Ru−O−Ti interface undergoes the considerable rotation of C═O axes in the gradual approaching C atom of carboxyl group. Compared to Ru (0 0 2), Ru/TiO_2 interfacial structure greatly decreases the activation energy to 0.48 eV for GVL − OH*

formation via $CH_3CHOCH_2CH_2COOH$* cyclization. For LA hydrogenation to GVL on Ru/TiO_2, LA hydrogenation to $CH_3CHOCH_2CH_2COOH$* is no longer a determining-rate step (0.26 eV), as is that on Ru (0 0 2). The bottleneck is associated with GVL − OH* formation via $CH_3CHOCH_2CH_2COOH$* cyclization (0.48 eV), and the corresponding energy barrier is much lower than that of Ru (0 0 2) (0.69 eV). Moreover, all the steps on Ru/TiO_2 need substantially lower activation energy barriers than those of Ru (0 0 2), thereby accelerating GVL formation. Such observation also agrees with the experimental results, showing that the excellent intrinsic activity for GVL synthesis is associated with the combination of Ru and TiO_2, namely the interfacial Ru−O−Ti structure. Thus, two-dimensional TiO_2 has abundant unsaturated Ti^{4+} bond in surface that easily bonds with Ru to form Ru−O−Ti interfacial structure, resulting in excellent performance for LA hydrogenation.

4. Conclusions

The ultrathin TiO_2 nanosheets have demonstrated to be an excellent support to fabricate highly dispersed Ru nanoparticles. Strong interfacial Ru−O−Ti structure has been observed by HRTEM and XPS. The Ru/TiO_2 catalyst showed exceedingly high activity for LA hydrogenation to GVL, and the GVL yield of 99.1% was achieved. Its TOF reached as high as 19,045 h^{-1} at 100 °C, much higher than those of Ru/SiO_2, Ru/GO, Ru/MoS_2, and commercial Ru/C, which is the highest value ever reported. DFT calculations confirm that LA hydrogenation to GVL undergoes preferential hydrogenation to $CH_3CHOCH_2CH_2COOH$*, cyclization to GVL-OH followed by dehydroxylation, irrespective of

surface structure. Compared to Ru (0 0 2) surface, Ru/TiO$_2$ interfacial structure changes the rate-determining step from initial hydrogenation to cyclization, which significantly decreases the activation barrier from 0.81 eV to 0.48 eV. The interfacial nature and optimum bonding of this nanosheet TiO$_2$-anchored Ru nanostructure confers the catalyst with outstanding LA hydrogenation activity and reusability. This work highlights the crucial role of metal/reducible oxide interface in enhancing reactivity of LA hydrogenation at the atomic level, and the insights achieved can hold wide potential applications in biomass conversion.

Declaration of Competing Interest

The authors declare that they have no known competing financial interests or personal relationships that could have appeared to influence the work reported in this paper.

Acknowledgements

Appendix A. Supplementary data

Supplementary material related to this article can be found, in the online version, at doi:https://doi.org/10.1016/j.apcatb.2019.118076.

References

[1] J. Zhang, S. Wu, B. Li, H. Zhang, ChemCatChem 4 (2012) 1230–1237.
[2] F.D. Pileidis, M.-M. Titirici, ChemSusChem 9 (2016) 562–582.
[3] L. Yan, Q. Yao, Y. Fu, Green Chem. 19 (2017) 5527–5547.
[4] K. Mudiyanselage, I. Al-Shankiti, A. Foulis, J. Llorca, H. Idriss, Appl. Catal. B: Environ. 197 (2016) 198–205.
[5] J.Q. Bond, D.M. Alonso, D. Wang, R.M. West, J.A. Dumesic, Science 327 (2010) 1110–1114.
[6] S. Zhu, Y. Xue, J. Guo, Y. Cen, J. Wang, W. Fan, ACS Catal. 6 (2016) 2035–2042.
[7] J.S. Luterbacher, J.M. Rand, D.M. Alonso, J. Han, J.T. Youngquist, C.T. Maravelias, B.F. Pfleger, J.A. Dumesic, Science 343 (2014) 277–280.
[8] J. Ftouni, A. Muñoz-Murillo, A. Goryachev, J.P. Hofmann, E.J.M. Hensen, L. Lu, C.J. Kiely, P.C.A. Bruijnincx, B.M. Weckhuysen, ACS Catal. 6 (2016) 5462–5472.
[9] J. Tan, J. Cui, X. Cui, T. Deng, X. Li, Y. Zhu, Y. Li, ACS Catal. 5 (2015) 7379–7384.
[10] C. Xiao, T.-W. Goh, Z. Qi, S. Goes, K. Brashler, C. Perez, W. Huang, ACS Catal. (2015) 593–599.
[11] M. Nemanashi, J.-H. Noh, R. Meijboom, Appl. Catal. A: Gen. 550 (2018) 77–89.
[12] C. Moustani, E. Anagnostopoulou, K. Krommyda, C. Panopoulou, K.G. Koukoulakis, E.B. Bakeas, G. Papadogianakis, Appl. Catal. B: Environ. 238 (2018) 82–92.
[13] J. Molleti, M.S. Tiwari, G.D. Yadav, Chem. Eng. J. 334 (2018) 2488–2499.
[14] A.M. Ruppert, J. Grams, M. Jedrzejczyk, J. Matras-Michalska, N. Keller, K. Ostojska, P. Sautet, ChemSusChem 8 (2015) 1538–1547.
[15] W. Zuojun, L. Jiongtao, S. Chuanmin, G. Dechao, L. Yingxin, D. Shuguang, ChemSusChem 10 (2017) 1720–1732.
[16] M.G. Al-Shaal, W.R.H. Wright, R. Palkovits, Green Chem. 14 (2012) 1260–1263.
[17] W. Cao, W. Luo, H. Ge, Y. Su, A. Wang, T. Zhang, Green Chem. 19 (2017) 2201–2211.
[18] A.M.R. Galletti, C. Antonetti, V. De Luise, M. Martinelli, Green Chem. 14 (2012) 688–694.
[19] S. Cao, J.R. Monnier, J.R. Regalbuto, J. Catal. 347 (2017) 72–78.
[20] S. Cao, J.R. Monnier, C.T. Williams, W. Diao, J.R. Regalbuto, J. Catal. 326 (2015) 69–81.
[21] G. Li, H. Yang, M. Cheng, W. Hu, L. Tian, W. Mao, R. Nie, Mol. Catal. 455 (2018) 95–102.
[22] Z. Wei, X. Li, J. Deng, J. Wang, H. Li, Y. Wang, Mol. Catal. 448 (2018) 100–107.
[23] K. Yan, T. Lafleur, G. Wu, J. Liao, C. Ceng, X. Xie, Appl. Catal. A: Gen. 468 (2013) 52–58.
[24] M. Sudhakar, V.V. Kumar, G. Naresh, M.L. Kantam, S.K. Bhargava, A. Venugopal, Appl. Catal. B: Environ. 180 (2016) 113–120.
[25] W. Cao, L. Lin, H. Qi, Q. He, Z. Wu, A. Wang, W. Luo, T. Zhang, J. Catal. 373 (2019) 161–172.
[26] B. Zhang, Y. Chen, J. Li, E. Pippel, H. Yang, Z. Gao, Y. Qin, ACS Catal. 5 (2015) 5567–5573.
[27] S. Ishikawa, D.R. Jones, S. Iqbal, C. Reece, D.J. Morgan, D.J. Willock, P.J. Miedziak, J.K. Bartley, J.K. Edwards, T. Murayama, W. Ueda, G.J. Hutchings, Green Chem. 19 (2017) 225–236.
[28] H. Zhou, J. Song, H. Fan, B. Zhang, Y. Yang, J. Hu, Q. Zhu, B. Han, Green Chem. 16 (2014) 3870–3875.
[29] S. Song, S. Yao, J. Cao, L. Di, G. Wu, N. Guan, L. Li, Appl. Catal. B: Environ. 217 (2017) 115–124.
[30] M. Sun, J. Xia, H. Wang, X. Liu, Q. Xia, Y. Wang, Appl. Catal. B: Environ. 227 (2018) 488–498.
[31] L. Wei, F. Guoli, Y. Lan, L. Feng, ChemCatChem 8 (2016) 2724–2733.
[32] D. Liu, L. Zhang, W. Han, M. Tang, L. Zhou, Y. Zhang, X. Li, Z. Qin, H. Yang, Chem. Eng. J. 369 (2019) 386–393.
[33] K.-i. Shimizu, S. Kanno, K. Kon, Green Chem. 16 (2014) 3899–3903.
[34] S.S.R. Gupta, M.L. Kantam, Catal. Today 309 (2018) 189–194.
[35] L. Zhang, J. Mao, S. Li, J. Yin, X. Sun, X. Guo, C. Song, J. Zhou, Appl. Catal. B: Environ. 232 (2018) 1–10.
[36] Y. Yang, G. Gao, X. Zhang, F. Li, ACS Catal. 4 (2014) 1419–1425.
[37] S.G. Wettstein, J.Q. Bond, D.M. Alonso, H.N. Pham, A.K. Datye, J.A. Dumesic, Appl. Catal. B: Environ. 117-118 (2012) 321–329.
[38] W. Luo, M. Sankar, A.M. Beale, Q. He, C.J. Kiely, P.C.A. Bruijnincx, B.M. Weckhuysen, Nat. Commun. 6 (2015) 6540.
[39] M.M. Kauppinen, M.M. Melander, A.S. Bazhenov, K. Honkala, ACS Catal. 8 (2018) 11633–11647.
[40] O. Mamun, E. Walker, M. Faheem, J.Q. Bond, A. Heyden, ACS Catal. 7 (2017) 215–228.
[41] O. Mamun, M. Saleheen, J.Q. Bond, A. Heyden, J. Phys. Chem. C 121 (2017) 18746–18761.
[42] S. Hu, P. Qiao, L. Zhang, B. Jiang, Y. Gao, F. Hou, B. Wu, Q. Li, Y. Jiang, C. Tian, W. Zhou, G. Tian, H. Fu, Appl. Catal. B: Environ. 239 (2018) 317–323.
[43] Y. Liu, C. Miao, P. Yang, Y. He, J. Feng, D. Li, Appl. Catal. B: Environ. 244 (2019) 919–930.
[44] X. Kong, Y. Xu, Z. Cui, Z. Li, Y. Liang, Z. Gao, S. Zhu, X. Yang, Appl. Catal. B: Environ. 230 (2018) 11–17.
[45] Y.-J. Yuan, Z.-J. Ye, H.-W. Lu, B. Hu, Y.-H. Li, D.-Q. Chen, J.-S. Zhong, Z.-T. Yu, Z.-G. Zou, ACS Catal. 6 (2015) 532–541.
[46] S. Zhu, Y. Cen, M. Yang, J. Guo, C. Chen, J. Wang, W. Fan, Appl. Catal. B: Environ. 211 (2017) 89–97.
[47] A.S. Piskun, J. Ftouni, Z. Tang, B.M. Weckhuysen, P.C.A. Bruijnincx, H.J. Heeres, Appl. Catal. A: Gen. 549 (2018) 197–206.
[48] G. Kresse, J. Furthmiiller, Comput. Mater. Sci. 6 (1996) 15–50.
[49] G. Kresse, J. Hafner, Phys. Rev. B 47 (1993) 558–561.
[50] J.P. Perdew, K. Burke, M. Ernzerhof, Phys. Rev. Lett. 77 (1996) 3865–3868.
[51] P.E. Blöchl, Phys. Rev. B 50 (1994) 17953–17979.
[52] G. Kresse, D. Joubert, Phys. Rev. B 59 (1999) 1758–1775.
[53] H.-Y.T. Chen, S. Tosoni, G. Pacchioni, ACS Catal. 5 (2015) 5486–5495.
[54] G. Henkelman, B.P. Uberuaga, H. Jónsson, J. Chem. Phys. 113 (2000) 9901–9904.
[55] G. Henkelman, H. Jónsson, J. Chem. Phys. 113 (2000) 9978–9985.
[56] T. Zhu, J. Li, S. Yip, Phys. Rev. Lett. 93 (2004) 025503.
[57] J. Lv, Z. Rong, L. Sun, C. Liu, A.-H. Lu, Y. Wang, J. Qu, Catal. Sci. Technol. 8 (2018) 975–979.
[58] B. Wu, C. Guo, N. Zheng, Z. Xie, G.D. Stucky, J. Am. Chem. Soc. 130 (2008) 17563–17567.
[59] S. Chen, A.M. Abdel-Mageed, D. Li, J. Bansmann, S. Cisneros, J. Biskupek, W. Huang, R.J. Behm, Angew. Chem. Int. Ed. (2019), https://doi.org/10.1002/anie.201903882.
[60] O.A. Abdelrahman, A. Heyden, J.Q. Bond, ACS Catal. 4 (2014) 1171–1181.
[61] V.K. Velisoju, G.B. Peddakasu, N. Gutta, V. Boosa, M. Kandula, K.V.R. Chary, V. Akula, J. Phys. Chem. C 122 (2018) 19670–19677.
[62] G.B. Peddakasu, V.K. Velisoju, M. Kandula, N. Gutta, K.V.R. Chary, V. Akula, Catal. Today 325 (2019) 68–72.
[63] J.E. De Vrieze, J.W. Thybaut, M. Saeys, ACS Catal. 8 (2018) 7539–7548.